JOURNAL OF PROPULSION AND POWER
Vol. 21, No. 2, March–April 2005

Aerodynamic Damping Predictions in Turbomachines Using a Coupled Fluid–Structure Model

Dana A. Gottfried* and Sanford Fleeter†
Purdue University, West Lafayette, Indiana 47907

Flow-induced vibration of turbomachine blade rows is a coupled fluid–structure problem. Thus, rather than separate fluid and structural models, a coupled interacting fluid–structures analysis is needed. This need is addressed by extending the finite element code ALE3D that solves the three-dimensional Euler equations to model the unsteady aerodynamics of turbomachine blade rows. The same finite element model is applied to both the blading and the fluid, which results in consistency between the fluid and structure. Such a coupled interacting fluid–structure analysis enables the aerodynamic damping of multiple vibration modes to be predicted from two time-domain simulations: one with the blading in a vacuum and one with the blading in flow. This novel approach to predict aerodynamic damping is demonstrated by the consideration of a modern transonic compressor blade row. The blading is first impulsed in its first bending and first torsion modes in a vacuum. It is then immersed in the design-point flowfield and impulsed in its first bending and first torsion modes again. Signal processing tools applied to the predicted blade response time history extract the difference in the decay rate of both modes.

Nomenclature

A	=	amplitude of response envelope
$\boldsymbol{A}$	=	speed of sound
$\boldsymbol{a}_i$	=	acceleration
$\boldsymbol{b}_i$	=	body force per unit volume
E	=	specific internal energy
F^{hg}	=	hourglass viscous force
f	=	impulse force coefficient
$\boldsymbol{h}_i$	=	hourglass deformation rate
M	=	mass of element
$\boldsymbol{n}_i$	=	normal pointing out of control surface
Q^{hg}	=	hourglass viscosity coefficient
q	=	shock smearing factor
S	=	surface of element
$\boldsymbol{t}$	=	time
$\boldsymbol{U}_i$	=	mesh velocity
$\boldsymbol{u}_i$	=	material velocity
$\mathcal{V}$	=	volume of element
$\boldsymbol{x}_i$	=	position vector
Γ	=	hourglass deformation basis vector
ε_{ijk}	=	alternating unit tensor
ζ_a	=	nondimensional damping constant due to aerodynamics only
ζ_{tot}	=	total nondimensional damping constant
ζ_v	=	nondimensional damping constant in vacuum
ρ	=	density
σ_{ij}	=	stress tensor
τ	=	pseudotime/damping time constant
ω_n	=	frequency

Subscripts

e	=	elemental value
I	=	nodal value, node number
i	=	spatial coordinate, 1, 2, 3
j	=	spatial coordinate, 1, 2, 3

Superscripts

n	=	time step level
$\prime$	=	dual-mesh element quantity

Received 20 August 2003; revision received 19 December 2003; accepted for publication 19 December 2003.

*Postdoctoral candidate, School of Mechanical Engineering.
†McAllister Distinguished Professor, School of Mechanical Engineering. Fellow AIAA.

Introduction

THERE has been great progress of turbomachine flow modeling over the past several decades. In the steady flow realm, the initial numerical methods, for example, panel methods, required little computer time and did an adequate job of modeling subsonic flows. Later, full Euler solvers enabled the modeling of transonic flows, but still did not address viscous and three-dimensional effects. Currently, designers use three-dimensional steady Navier–Stokes solvers during the final stages of blade design.

Models for unsteady flow in turbomachinery have lagged behind the steady flow models because of their added complexity. However, their development is crucial because turbomachine blade rows operate in an inherently unsteady environment. The unsteady aerodynamic loading on the blading due to both flutter and forced response is the root cause for high cycle fatigue blade failure. Thus, there is an urgent need to predict this unsteady aerodynamic loading and use the predictions to design more reliable and durable turbomachinery blade rows.

For blade-motion unsteadiness, either the unsteadiness can be specified a priori as a boundary condition to the aerodynamics, or the aerodynamics and structure can be modeled simultaneously, as in a coupled fluid–structure interaction problem. In the infancy of this field, the former was chosen due to its relative simplicity. One moves closer to full fluid–structure interaction by modeling the blade as a beam. In this approach, there are two separate systems of equations being solved: the structural system and the fluid system. They are coupled only in that the aerodynamic forces and blade state are passed between each other after each time step. This pseudocoupling approach produces phase-lagging errors that can act as energy sources or sinks in the system.

Fluid–structure interaction that more precisely models the energy exchange between the fluid and structure can be obtained by modeling both the fluid and structure with consistent numerical schemes. Bendiksen[1,2] accomplished this by solving the Euler equations using a finite volume method and the structural equations by a finite element method that used solid elements with bilinear shape functions. The final integral conservation law form of the fluid and structural equations are similar, and thus, both can be marched forward in time using the same five-stage Runge–Kutta technique. These

results showed superior modeling of the energy exchange between the fluid and the structure.

This research begins to address the need for a three-dimensional coupled fluid–structure interaction model for turbomachine blade rows appropriate for all flow regimes with no phase-lagging errors. Namely, a finite element model able to handle both fluids and solids has been developed at Lawrence Livermore National Laboratories. This code, arbitrary Lagrangian–Eulerian/3D (ALE3D), was developed from the DYNA3D model[3] with the added capability to handle general fluid–structure interaction problems, especially those involving plastic deformations. Phenomena can be modeled from the Lagrangian or Eulerian perspectives, or from any arbitrary reference frame. This approach is well suited for fluid–structure interaction problems where the structure is best modeled from the Lagrangian perspective, whereas the fluid is typically modeled from the Eulerian point of view. Because the same finite element method is used for the fluid and the structure, phase-lagging errors are minimized.

Unfortunately ALE3D cannot be directly applied to fluid–structure interaction problems in the turbomachinery environment. Modifications are necessary to include appropriate turbomachine blade and flow mesh algorithms. In particular, periodic boundary conditions must be added to the sides of the domain so that only one blade passage needs to be analyzed. The hub and tip of the flow passage must be modified so that there is no fluid velocity normal to these curved surfaces. The inflow boundary must be modified to allow for variable inflow velocity. Appropriate routines to output blade surface pressures at various sections, mass flow rate, and other mass-averaged properties are also necessary additions to the code. The resulting turbomachinery aeromechanics code is called TAM-ALE3D, with its ability to model unsteady turbomachinery aerodynamics validated.[4]

This paper is directed at developing and implementing a technique to predict the aerodynamic damping of multiple vibration modes from two time-domain flow simulations. This is accomplished by first impulsing the blading in a vacuum and recording its response. The blading is then inserted into the design-point flowfield and impulsed again. The aerodynamic damping in individual modes is then predicted by applying signal-processing tools to the predicted blade response time histories.

The steel rotor blades of a modern-design transonic compressor rotor are modeled by the finite element analysis, with dynamic experiments performed with the code. First the blade is simulated as rotating at 20,000 rpm in a vacuum and the first two vibratory modes (first bending and first torsion) are quantified by impulsing the blade in these modes. The rotor blade is then considered in a flow corresponding to the compressor design point, and the analysis is performed in three steps. First, the blade is fixed and the flow is marched to a steady-state condition that matches the design mass flow rate. Next, the blade is allowed to move and dynamically relax to a steady-state condition. The influence of centripetal acceleration and air pressure causes the blade's steady state geometry to be different from its geometry in a vacuum without rotation. Finally, the blade is impulsed and the time-history of the response is compared to its time history when the blade is impulsed in a vacuum. This comparison gives the aerodynamic damping for both the first bending and first torsion modes.

Mathematical Model

The equations describing a system specify conservation of mass, momentum, and energy. The position of a finite volume with volume $\mathcal{V}$ having a surface S is

$$S(\boldsymbol{x}_i, t) = 0 \tag{1}$$

where $\boldsymbol{x}_i$ is the position vector with i representing the three coordinate directions.

Equation (1) specifies that a point P with position $\boldsymbol{x}_i$ at time t is on the surface of the volume. The motion of the volume can be different from that of the continuum and different from zero. Thus, the volume does not constitute a material volume, but rather a control volume that moves relative to the fixed reference frame. The motion of the volume is specified by the velocity $\boldsymbol{U}_i$ of the boundary S, that is, $\boldsymbol{U}_i = \partial \boldsymbol{x}_i / \partial t$.

The conservation laws of mass, momentum, and energy for the volume $\mathcal{V}$ of the continuum enclosed by S are

$$\frac{\mathrm{d}}{\mathrm{d}t}\int_{\mathcal{V}} \rho \,\mathrm{d}\mathcal{V} + \int_S \rho(\boldsymbol{u}_i - \boldsymbol{U}_i)\boldsymbol{n}_i \,\mathrm{d}S = 0 \tag{2}$$

$$\frac{\mathrm{d}}{\mathrm{d}t}\int_{\mathcal{V}} \rho \boldsymbol{u}_i \,\mathrm{d}\mathcal{V} + \int_S \rho \boldsymbol{u}_i(\boldsymbol{u}_j - \boldsymbol{U}_j)n_j \,\mathrm{d}S = \int_S (\boldsymbol{n}_j \sigma_{ji} - q\boldsymbol{n}_i)\,\mathrm{d}S + \int_{\mathcal{V}} \rho \boldsymbol{b}_i \,\mathrm{d}\mathcal{V} \tag{3}$$

$$\frac{\mathrm{d}}{\mathrm{d}t}\int_{\mathcal{V}} \rho E \,\mathrm{d}\mathcal{V} + \int_S \rho E(\boldsymbol{u}_i - \boldsymbol{U}_i)\boldsymbol{n}_i \,\mathrm{d}S = \int_{\mathcal{V}} (\sigma_{ij} u_{i,j} - q u_{i,i})\,\mathrm{d}\mathcal{V} \tag{4}$$

where the scalar variables ρ and E are the density and specific internal energy; i and j range from 1 to 3, with repeated indices summed per the rules of summation notation; $u_{i,j}$ is a convenient representation of the velocity gradient tensor, with the $,j$ subscript representing the derivative with respect to the j direction; $\boldsymbol{n}_i$ is the normal surface vector pointing out of the volume; σ_{ij} is the stress tensor; $\boldsymbol{b}_i$ is the body force per unit mass; and the q term is a mathematical device that smears shocks over distances comparable to the mesh interval in numerical calculations.[4,5]

To solve these equations, an operator split is performed to separate the problem into simpler parts: a Lagrangian part and an advection part. Specifically, the velocity of the mesh is split into two parts: $\boldsymbol{U}_i = \boldsymbol{U}_i^{(1)} + \boldsymbol{U}_i^{(2)}$. In the first part of the operator split, $\boldsymbol{U}_i^{(1)} = \boldsymbol{u}_i$, which allows the mesh to move with the material according to the equations of motion. In the second part, the motion of the system is frozen, but the mesh is moved through the domain by setting $\boldsymbol{U}_i^{(2)} = \boldsymbol{U}_i - \boldsymbol{u}_i$. The first step is called the Lagrangian step, whereas the second step is referred to as the advection step.

The equations of motion for the Lagrangian step are found by substituting $\boldsymbol{U}_i = \boldsymbol{U}_i^{(1)} = \boldsymbol{u}_i$ into the conservation equations,

$$\frac{\mathrm{D}}{\mathrm{D}t}\int_{\mathcal{V}} \rho \,\mathrm{d}\mathcal{V} = 0 \tag{5}$$

$$\frac{\mathrm{D}}{\mathrm{D}t}\int_{\mathcal{V}} \rho \boldsymbol{u}_i \,\mathrm{d}\mathcal{V} = \int_S (\boldsymbol{n}_j \sigma_{ji} - q\boldsymbol{n}_i)\,\mathrm{d}S + \int_{\mathcal{V}} \rho \boldsymbol{b}_i \,\mathrm{d}\mathcal{V} \tag{6}$$

$$\frac{\mathrm{D}}{\mathrm{D}t}\int_{\mathcal{V}} \rho E \,\mathrm{d}\mathcal{V} = \int_{\mathcal{V}} (\sigma_{ij} u_{i,j} - q u_{i,i})\,\mathrm{d}\mathcal{V} \tag{7}$$

where D/Dt shows that the finite volume is moving with the material.

In the second step of the operator split, real time is fixed, the system is frozen, and the mesh is moved through the field with the velocity $\boldsymbol{U}_i^{(2)} = \boldsymbol{U}_i - \boldsymbol{u}_i$. This can be thought of as merely a geometric update of the mesh, so that the right-hand-side source terms in Eqs. (2–4) are set to zero and the flow velocity $\boldsymbol{u}_i$ in the flux term is zero. However, the $\boldsymbol{u}_i$ term appearing in $\boldsymbol{U}_i^{(2)}$ is still necessary to account for the motion of the mesh during its relaxation. Because real time is not progressing during the advection step (where the material is frozen), a pseudotime τ is introduced that advances during this second part of the operator split. The advection equations in pseudotime are then

$$\frac{\mathrm{d}}{\mathrm{d}\tau}\int_{\mathcal{V}} \rho \,\mathrm{d}\mathcal{V} + \int_S \rho(\boldsymbol{u}_i - \boldsymbol{U}_i)\boldsymbol{n}_i \,\mathrm{d}S = 0 \tag{8}$$

$$\frac{\mathrm{d}}{\mathrm{d}\tau}\int_{\mathcal{V}} \rho u_i \,\mathrm{d}\mathcal{V} + \int_S \rho \boldsymbol{u}_i(\boldsymbol{u}_j - \boldsymbol{U}_j)\boldsymbol{n}_j \,\mathrm{d}S = 0 \tag{9}$$

$$\frac{\mathrm{d}}{\mathrm{d}\tau}\int_{\mathcal{V}} \rho E \,\mathrm{d}\mathcal{V} + \int_S \rho E(\boldsymbol{u}_i - \boldsymbol{U}_i)\boldsymbol{n}_i \,\mathrm{d}S = 0 \tag{10}$$

Space and Time Discretizations

The computational domain is discretized using an unstructured assembly of hexahedron (six-sided) elements. The fundamental

unknowns are assigned to staggered locations in the mesh. The stress tensor, specific internal energy, mass, and shock-smearing factor are assigned to element centers, with these constant over the element. The flow and mesh velocities $\boldsymbol{u}_i$ and $\boldsymbol{U}_i$ are assigned to element nodes. In the time discretization, the unknowns are also staggered. The stress tensor, internal energy, and density are evaluated at time levels $n, n+1, n+2, \ldots$, whereas the flow and mesh velocities are evaluated at time levels $n-\frac{1}{2}, n+\frac{1}{2}, n+\frac{3}{2}, \ldots$.

The equations are discretized by choosing integration volumes as those of the finite elements. Furthermore, because the velocities are defined at element nodes, integrating the momentum equations (6) and (9) requires the use of a dual-mesh element, which is defined by a hexahedron whose vertices are at the center of the surrounding elements. Here $\mathcal{V}'$, S', and $\boldsymbol{n}_i'$ are the volume, surface, and surface normal of this dual-mesh element.

Marching Forward in Time

For each time step there is a Lagrange calculation, a relaxation of the mesh, and an advection calculation, in this order. All three calculations must be performed for the fluid elements, with only the Lagrange calculation necessary for the structural elements.

Lagrange Calculation

In the first part of the operator split, $\boldsymbol{U}_i^{(1)}$ is set equal to $\boldsymbol{u}_i$ and Eqs. (5–7) are marched forward in real time.

Equation (5) shows that mass is constant in the volumes $\mathcal{V}$ and $\mathcal{V}'$. The mass M' in the dual-mesh element is one-eighth the sum of the masses of the surrounding elements. Using the dual-mesh element to integrate Eq. (6) then yields

$$\left(M'\boldsymbol{a}_i^n\right)_I = \sum_e \left[\boldsymbol{n}_j'\left(\sigma_{ji}^n\right)_e - \left(q^{n-\frac{1}{2}}\right)_e \boldsymbol{n}_i'\right]\Delta S' + \left(M'\boldsymbol{b}_i^n\right)_I \quad (11)$$

where the superscript denotes the time level, the subscript I denotes node I, with the subscript e denotes element e. The summation is over all elements surrounding node I, with eight elements for an interior node or four, two, or one element for a boundary node, and $\Delta S'$ is the fraction of surface area of the dual-mesh element contained in element e.

For a reference frame rotating at a constant angular velocity $\boldsymbol{\omega}_i$, the body force per unit mass includes both Coriolis and centripetal accelerations,

$$b_i^n = -2\varepsilon_{ijk}\omega_j u_k^{n-\frac{1}{2}} - \varepsilon_{ijk}\omega_j\left(\varepsilon_{klm}\omega_l x_m^n\right) \quad (12)$$

Here ε_{ijk} is the alternating unit tensor that has the effect of taking the cross product of two vectors[6] and $\boldsymbol{x}_m^n$ is the position vector at time level n. For example, if the angular velocity is along the 3 axis, the body force per unit mass is

$$b_1^n = \left(x_1^n\omega + 2u_2^{n-\frac{1}{2}}\right)\omega \qquad b_2^n = \left(x_2^n\omega - 2u_1^{n-\frac{1}{2}}\right)\omega \qquad b_3^n = 0 \quad (13)$$

Application of Eq. (11) gives the nodal accelerations at time level n. However, the equation must be modified to incorporate the hourglass viscous damping.

Hourglass Viscosity

For a hexahedron element, there are eight degrees of freedom in each coordinate direction, one for each node. A set of basis vectors for an eight-degree-of-freedom system is given in Table 1. These can be interpreted as the eight deformation modes of a hexahedron element. Representations of the eight deformation modes corresponding to these basis vectors are given in Fig. 1. Γ_{Ik} denotes the eight-component vector describing each hourglass mode, where I corresponds to the eight nodes of the element and k corresponds to the four hourglass modes. The rigid-body mode and the hourglass modes are unique in that they result in no net change in the volume of the element.

Table 1 Deformation modes of a hexahedron element

Deformation mode	Node number I							
	1	2	3	4	5	6	7	8
Rigid body Σ_I	1	1	1	1	1	1	1	1
Expansion/contraction Λ_{I1}	−1	1	1	−1	−1	1	1	−1
Shear 1 Λ_{I2}	−1	−1	1	1	−1	−1	1	1
Shear 2 Λ_{I3}	1	1	1	1	−1	−1	−1	−1
Hourglass 1 $\boldsymbol{\Gamma}_{I1}$	−1	−1	1	1	1	1	−1	−1
Hourglass 2 $\boldsymbol{\Gamma}_{I2}$	−1	1	1	−1	1	−1	−1	1
Hourglass 3 $\boldsymbol{\Gamma}_{I3}$	1	−1	1	−1	1	−1	1	−1
Hourglass 4 $\boldsymbol{\Gamma}_{I4}$	1	−1	1	−1	−1	1	−1	1

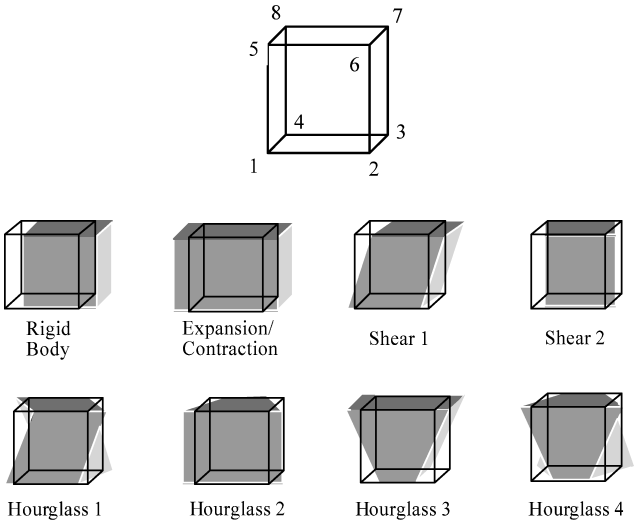

Fig. 1 Element nodal numbering and hexahedron element deformation modes.

The strain of the elements is approximated as constant over the element. Thus, deformations resulting in no net volume change produce no change in the strain of the element. Because the strain state is not affected by these deformation modes, the stress state is also not affected, and the four hourglass modes have no natural mechanism whereby they are resisted. Small numerical errors could create deformations in these hourglass modes, which, left unresisted, would destroy the solution. Although the rigid-body mode also has no net volume change, it is resisted by the global boundary conditions.

Such numerically generated hourglass modes are often oscillatory with smaller periods than that of the physical process.[7] Thus, a good way of resisting them is to apply an artificial viscous force in these deformation modes. First, with use of the velocity, the extent to which the element is deforming in the hourglass modes is calculated,

$$\boldsymbol{h}_{ik} = \boldsymbol{u}_{iI}\boldsymbol{\Gamma}_{Ik} \quad (14)$$

where $\boldsymbol{h}_{ik}$ is the rate at which an element is deforming in hourglass mode k in the three i coordinate directions.

An hourglass resisting force for each element is then taken to be proportional to $\boldsymbol{h}_{ik}$ and distributed among the nodes so that it is applied in the shape of the hourglass mode. This hourglass resisting force is

$$\boldsymbol{F}_{iI}^{\text{hg}} = -\rho\mathcal{V}^{\frac{2}{3}}\left[0.25Q^{\text{hg}}\boldsymbol{A} + 25(Q^{\text{hg}})^2|\boldsymbol{h}_{ik}|\right]\boldsymbol{h}_{ik}\boldsymbol{\Gamma}_{Ik} \quad (15)$$

where there is no summation over i although this subscript is repeated on the right-hand side, Q^{hg} is the user-specified constant usually set between 0.05 and 0.15, in nomenclature, and $\boldsymbol{A}$ is the material speed of sound.

The viscous hourglass force is added to the nodal forces calculated in Eq. (11). Thus, the acceleration of a node is

$$\left(M'\boldsymbol{a}_i^n\right)_I = \sum_e \left[\boldsymbol{n}_j'\left(\sigma_{ji}^n\right)_e - \left(q^{n-\frac{1}{2}}\right)_e \boldsymbol{n}_i'\right]\Delta S' + \left(M'\boldsymbol{b}_i^n\right)_I + \boldsymbol{F}_{iI}^{\text{hg}} \quad (16)$$

Update All Nodal Positions and Velocities

After the nodal accelerations are obtained, a centered-difference formula is used to find the velocity at time level $n+\frac{1}{2}$. The centered-difference formula is again applied to find the new position of the node at time level $n+1$, that is,

$$\boldsymbol{u}_i^{\,n+\frac{1}{2}} = \boldsymbol{u}_i^{\,n-\frac{1}{2}} + \Delta t^{n-\frac{1}{2}} \boldsymbol{a}_i^n \tag{17}$$

$$\boldsymbol{x}_i^{\,n+1} = \boldsymbol{x}_i^n + \Delta t^n \boldsymbol{u}_i^{\,n+\frac{1}{2}} \tag{18}$$

where Δt^n is the time step from time level n to level $n+1$. The time step from $n-\frac{1}{2}$ to $n+\frac{1}{2}$ is calculated from this as $\Delta t^{n-1/2} = 0.5(\Delta t^n + \Delta t^{n-1})$, and provision for $\Delta t^n \neq \Delta t^{n-1/2}$ is necessary because the time step is allowed to vary throughout the simulation.

The maximum time step for the simulation is calculated at each step as that which satisfies the Lagrangian time step restriction and the advection time step restriction. The Lagrangian restriction says the time step must be small enough that during the step a disturbance propagating at the speed of sound moves no farther than the minimum of the characteristic lengths of the elements. The characteristic length of an element is taken as the volume of the element divided by the area of the largest of its six faces. In this study, the maximum time step is always limited by the Lagrangian time step because the speed of sound in the metal blade is more than an order of magnitude larger than that in air. The fluid simulation by itself does not need to run with such a small time step, but it is necessary to do so to capture the full fluid–structure interaction effect.

With such a small time step, excessive damping in the fluid from artificial viscosity is a possible concern. This has been studied for a case where a disturbance was propagated downstream through an annulus having axial of Mach 0.54 (Ref. 4). The decay of a 7200-Hz harmonic disturbance was observed for simulations with a time step close to the Courant–Friedrichs–Lewy (CFL) limit and a time step 31 times smaller than this. Within a distance of 5 cm, the approximate length of the domain used in the present study, the amplitude decayed by 1.7 and 2.0% using the larger and smaller time steps, respectively. Thus, using a time step much smaller than the CFL limit does not significantly damp the fluid dynamics.

Updating Elemental Values

The final part of the Lagrange calculation is to update the elemental values. Because it is a Lagrange calculation, the mass of the element does not change. However, the stress tensor, internal energy, and shock-smearing factor are changed. The stress tensor is updated in two steps. First, the rotation of the element is taken into account by rotating the stress tensor. Second, the elemental strain rate changes the stress tensor through constitutive relations. The constitutive relations used for the blade are those for a linear elastic isotropic solid. The elemental energy is updated by application of Eq. (7), and the shock-smearing factor is updated according to its governing equation.[4]

Mesh Relaxation and Advection

The Lagrange step is now complete, and all fluid and structural quantities are known at the $n+\frac{1}{2}$ and $n+1$ time levels. However, the fluid mesh cannot continue moving in a Lagrangian fashion, otherwise the solution will be destroyed as the mesh exits the solution domain with the fluid. Therefore, before proceeding to the next time level, it is necessary to relax the fluid mesh to a new position and calculate new fluid mesh quantities via an advection calculation.[4]

Boundary Conditions

Fluid–Structure Boundary

The interfaces between materials are termed slide surfaces, with the structural side called the master slide surface, and the fluid side the slave slide surface. A great convenience of the TAM-ALE3D code is that the master and slave nodes do not need to be adjacent. Interpolation is used to find the mass and acceleration of the region adjacent to a given slide surface node for proper application of the boundary condition.

For illustration, consider adjacent fluid and structural nodes. Before application of the fluid–structure boundary condition, these nodes are accelerating according to Eq. (16) without regard to each other's presence. The fluid–structure boundary condition then modifies the acceleration of these two nodes by requiring them to move together as one body normal to the interface. If the mass and acceleration of the slave and master nodes after application of Eq. (16) are M^{slave}, $\boldsymbol{a}_i^{\text{slave}}$ and M^{master}, $\boldsymbol{a}_i^{\text{master}}$, then the new acceleration normal to the slide surface for both nodes is

$$a_{\text{normal}}^{\text{new}} = \left(\frac{M^{\text{slave}} \boldsymbol{a}_i^{\text{slave}} + M^{\text{master}} \boldsymbol{a}_i^{\text{slave}}}{M^{\text{slave}} + M^{\text{master}}} \right) \boldsymbol{n}_i \tag{19}$$

where $\boldsymbol{n}_i$ is the unit vector normal to the slide surface.

This new acceleration is the acceleration of the combined fluid–structure boundary node, having mass $M^{\text{slave}} + M^{\text{master}}$. The acceleration from Eq. (16) is adjusted to reflect this change in normal acceleration. The velocity and position of the fluid nodes are calculated with Eqs. (17) and (18) with use of this new acceleration. They are then adjusted to account for the possibility that the blade surface is curved. At the new nodal positions, the nodes are required to be on the blade surface and the velocities are required to be tangent to the blade surface.

Only one blade passage is analyzed, with the flow variables transferred directly between the blade-to-blade boundaries. This corresponds to a 0-deg interblade phase angle.

The blade nodes at the hub are fixed with zero acceleration, whereas the tip blade nodes have no constraint on their motion. Most fluid nodes at the hub/tip boundaries are required to have zero velocity and displacement normal to the hub/tip surface. However, this constraint is not enforced for those fluid nodes on the tip of the blade surface. This special treatment is necessary because there is no tip clearance model. The tip of the blade lies exactly on the tip annulus boundary when the blade is stationary. However, when the blade is vibrating, the tip of the blade is free to move off the tip annulus wall. The fluid nodes on the blade tip surface remain on the blade surface, which results in a nonzero displacement normal to the tip annulus boundary. Their velocities are required to be tangent to the tip surface and to the blade.

At the inflow boundary, the flow velocity, density, and energy are specified, with the static pressure specified at the outflow boundary. This overspecifies the problem. However, consistency is obtained by varying the static pressure at the exit until the average density and internal energy of the elements along the inflow boundary match the specified density and energy. Note that both inflow and outflow boundary conditions are reflective.

Results

The aerodynamic damping of the first two vibration modes of a modern transonic compressor rotor with 18 blades and a design speed of 20,000 rpm is analyzed with this full fluid–structure interaction simulation. The steel blades have a Young's modulus of 2.06 Mbars, a Poisson's ratio of 0.28, and a density of 7830 kg/m^3. The geometry and properties of the steel blades, as well as the properties of the surrounding fluid flow for one blade passage, are modeled by the finite element analysis. Periodic boundaries are employed so that only one blade passage needs to be modeled.

The fluid–structure interaction simulation requires the simultaneous modeling of both the fluid and the structure using the same finite element method. Because the speed of sound in steel is over an order of magnitude larger than that in air, the maximum time step of the fluid–structure simulation must be over an order of magnitude less than that of a typical fluid-only simulation. This places a heavy burden on computational resources, and thus, every effort is made to reduce the size of the three-dimensional finite element mesh without severely compromising the integrity of the solution.

Figure 2 shows the finite element mesh used for the blade. There are 532 elements modeling the steel blade. Figure 3 shows a two-dimensional slice of the tip section of the blade, including the fluid mesh. The mesh is coarse around the leading and trailing edges so that the solution can be run in reasonable time. The full three-dimensional fluid mesh has 7986 hexahedron elements. With this

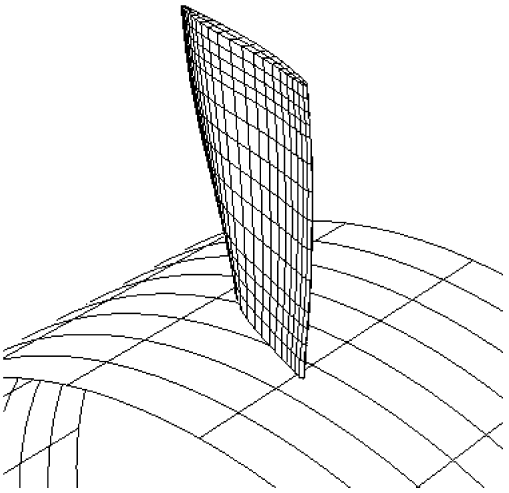

Fig. 2 Rotor blade finite element mesh.

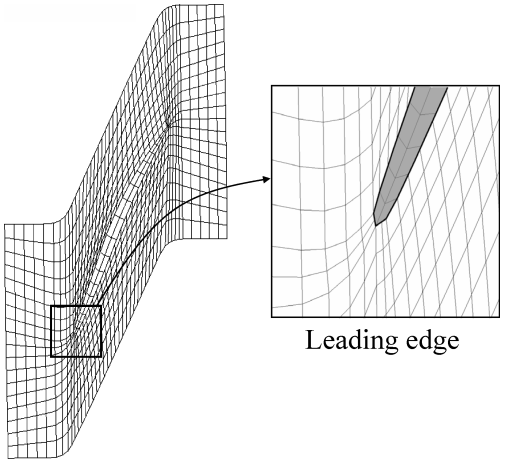

Fig. 3 Finite element mesh for the fluid and steel blade at blade tip.

coarse mesh, the three-dimensional steady flow Euler solution is obtained in 8 h of computer time on an IBM RS/6000. For the simulation of fluid–structure interaction, which includes the modeling of the steel blade, approximately one day of computer time is required to model one oscillation in the first bending mode.

Impulses

The behaviors of the first bending and first torsion modes are determined by impulsing the blade such that it oscillates predominately in these modes. The natural frequencies and decay rates are then extracted from the time history of the blade response.

The impulse is a force distributed over the nodes embedded halfway through the blade thickness. This force is applied for 100 μs and has a shape that approximates either the first bending mode or the first torsion mode. For both the bending and the torsion impulse, the maximum force amplitude $f = 5$ N, which results in noticeable blade tip displacement, but does not plastically deform the blade.

The first bending mode impulse, applied normal to the tip chord, has the shape

$$f[1 - \cos(y\pi/2)] \tag{20}$$

where y is the spanwise coordinate, 0 at the blade hub and 1 at the blade tip.

The first torsion mode impulse is applied normal to the tip chord and has the shape

$$f[1 - \cos(y\pi/2)]\xi \tag{21}$$

where ξ is the chordwise coordinate, -1 at the leading edge and $+1$ at the trailing edge.

Filtering to Extract Individual Modal Responses

The displacement time histories of a point on the blade tip leading edge are shown in Figs. 4 and 5 for the bending impulse and the torsion impulse at 0 rpm and 20,000 rpm in a vacuum. The effect of rotation is taken into account by including centripetal and Coriolis acceleration terms in the body force term $\boldsymbol{b}_i$ for rotation about the 3 axis. The nonsymmetric nature of the response for the torsion impulse is due to the first bending mode that is still present in the response. The response due to only the torsion mode is obtained by filtering the signal, accomplished by transforming the tip leading-edge displacement to the frequency domain via a Fourier transform.

Figure 6 shows the frequency-domain response of the blade rotating in a vacuum at 20,000 rpm and receiving a torsion impulse. The bending mode is apparent at 1310 Hz. The cutoff for filtering is chosen as that frequency having the lowest power spectral density between the two frequency peaks. The individual modal responses are then transformed back to the time domain via an inverse Fourier transform.

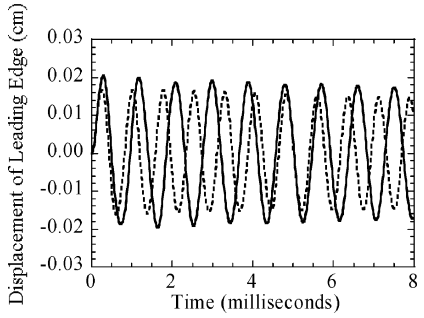

Fig. 4 Blade tip responses in a vacuum for bending impulse: ——, 0 rpm and – – –, 20,000 rpm.

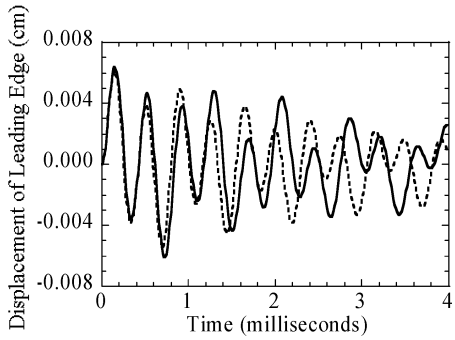

Fig. 5 Blade tip responses in a vacuum for torsion impulse: ——, 0 rpm and – – –, 20,000 rpm.

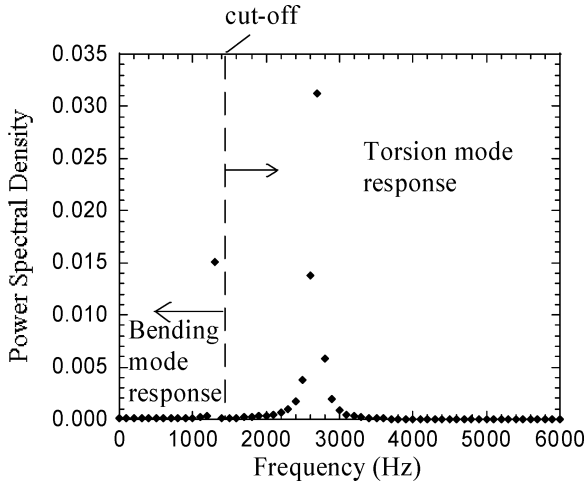

Fig. 6 Frequency response to torsion only impulse of rotating blade in vacuum.

Table 2 Predicted blade natural frequencies

	First bending		First torsion	
RPM	Frequency, Hz	Standard deviation, Hz	Frequency, Hz	Standard deviation, Hz
0	1110	10	2590	30
10,000	1160	31	2610	35
20,000	1310	13	2670	21

Table 3 Predicted steady-state blade tip displacements

	Displacement normal to chord, cm	
Position	In vacuum	In flow[a]
Leading edge	0.0059	0.0104
Midchord	0.0036	0.0080
Trailing edge	0.0008	0.0040

[a]At 20,000 rpm.

Natural Frequencies

Simulations are performed for the blade in a vacuum rotating at three different rotational speeds: 0, 10,000 and 20,000 rpm. For nonzero revolutions per minute, the blade is first dynamically relaxed to a steady state before it is impulsed. The relaxation is necessary to remove the transients caused by impulsively starting the blade rotation.

The resulting time histories of the blade tip leading-edge displacement normal to the chord are filtered using the filtering technique already presented to isolate the individual modal responses. The peaks and troughs of the filtered signals are then extracted, with the inverse of the average time between them giving the natural frequency of the mode.

For the bending mode, peaks and troughs are sampled from 2 to 8 ms. For the torsion mode, they are sampled from 1 to 4 ms. This sampling assures that at least 15 data points are used to compute the average natural frequency. The dependence of natural frequency on rotation rate is summarized in Table 2, along with the standard deviation of the results. To assure that mesh resolution is not an issue, TAM-ALE3D predictions were obtained with double the number of elements in the chordwise and spanwise directions. The resulting natural frequencies had negligible change.

Steady Flow Solution

The aerodynamic input parameters correspond to the rotor design operating point, where the rotor speed is 20,000 rpm and the mass flow rate is 5.216 kg/s. The distribution of relative flow velocity at the inflow boundary is also specified by design. The inflow stagnation properties in the nonrotating frame are set to standard temperature and pressure. The exit static pressure is set to give the proper mass flow rate.

With an exit static pressure of 1.227×10^5 Pa, the resulting mass flow rate at the inflow and outflow boundaries are 5.234 kg/s and 5.225 kg/s. The mass-averaged total pressure in the absolute frame at the inflow boundary is 1.020×10^5 Pa, which is less than 1% different from the standard pressure of 1.013×10^5 Pa. This indicates that the exit static pressure value is consistent with the specified inflow properties. The resulting mass-averaged total pressure at the outflow boundary is 1.354×10^5 Pa, yielding a total pressure ratio across the rotor of 1.33, which is the design value.

As the steady flow is established, the blade is held fixed in its initial position. The blade is then released and allowed to relax to a steady-state position under the influence of the external air pressure and the 20,000-rpm centripetal forces. The blade is numerically stopped at several instants to help the blade relax more quickly. The displacement of the tip of the blade normal to the chord in its steady-state position is shown in Table 3. Also shown are the analogous results for the blade in a vacuum, which includes centripetal acceleration effects only. Positive displacements are toward the suction side of the blade, so that the results show that both the air pressure and the centripetal acceleration cause the blade to bend more toward its suction side. The displacement of the blade from its initial position is so small that there is no noticeable change in the steady aerodynamics as the blade relaxes to its new steady-state position.

Aerodynamic Damping

There is both aerodynamic and nonaerodynamic damping present as the blade vibrates in the flowfield. The nonaerodynamic damping is due to the hourglass viscosity necessary to resist the unwanted hourglass modes. This damping is present even if the blade is vibrating in a vacuum. In this sense, the hourglass damping is similar to mechanical damping present in real blades due to the blade–disk interface and the internal energy dissipation sources. However, the hourglass damping is not intended to model real damping sources.

The aerodynamic and nonaerodynamic damping of each mode is evaluated in terms of the nondimensional decay constants ζ_a and ζ_v. If $f(t)$ is the undamped response, then the damped response in a vacuum is $\exp(-t\omega_n\zeta_v)f(t)$, where ω_n is the mode natural frequency. The damped response in the flow includes damping from both the hourglass viscosity and the aerodynamics. Thus, the response in flow is $\exp[-t\omega_n(\zeta_a+\zeta_v)]f(t)$. The total nondimensional damping parameter measured from the response of the blade in flow is $\zeta_{\text{tot}} = \zeta_a + \zeta_v$. Because both ζ_{tot} and ζ_v are measured quantities, the damping due to just the aerodynamics is

$$\zeta_a = \zeta_{\text{tot}} - \zeta_v \tag{22}$$

The response envelope for the blade in a vacuum is $A\exp(-t\omega_n\zeta_v)$, and that for the blade in flow is $A\exp(-t\omega_n\zeta_{\text{tot}})$. Because the duration of the impulse is very short (100 μs), the initial response amplitude is fixed regardless of whether the blade is impulsed in a vacuum or a flow. Therefore, the amplitude A used in the curve fit is first approximated by performing the curve fit with both A and ζ as parameters. The average A from the in-vacuum and inflow cases is then used as a fixed value in the second pass of the curve fit, which has only ζ as a parameter. This second-pass value of ζ is what is presented.

The amount of damping is also expressed in terms of a time decay constant τ, where the damping envelope follows $Ae^{-t/\tau}$. The τ value is calculated in the curve fit and is shown in the results. This value is related to ζ via $\zeta = 1/(\omega_n\tau)$.

Bending-Only Impulse

The aerodynamic damping is calculated for the first bending mode. After the blade reaches its steady-state position at 20,000 rpm, it is hit with the bending mode impulse, Eq. (20). The resulting displacement of the tip leading edge normal to the tip chord is shown in Fig. 7 for both the in-vacuum and the inflow cases. The computer time required for the in-vacuum case is approximately 4h/0.01 s of simulation, whereas for the inflow case it is 400 h/0.01 s of simulation.

The peaks and troughs of the curves within the interval 0.001 to 0.01 s are extracted, and a curve fit is passed through them (Fig. 7).

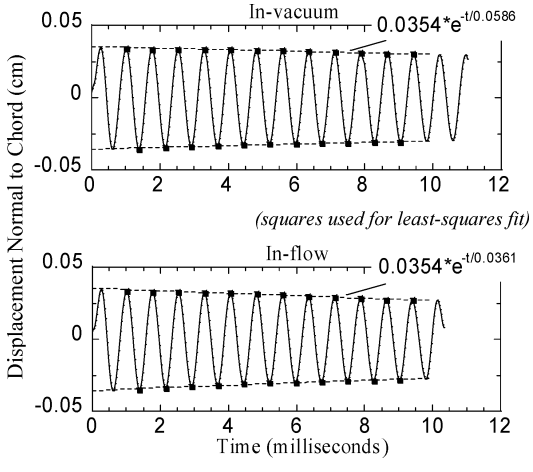

Fig. 7 Tip leading-edge displacement for bending-only impulse.

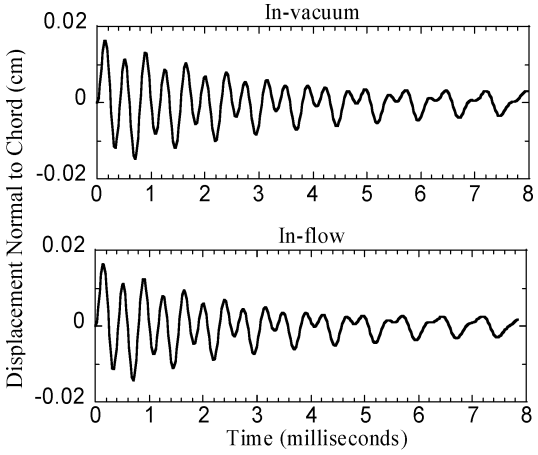

Fig. 8 Tip leading-edge displacement for torsion-only impulse before filtering.

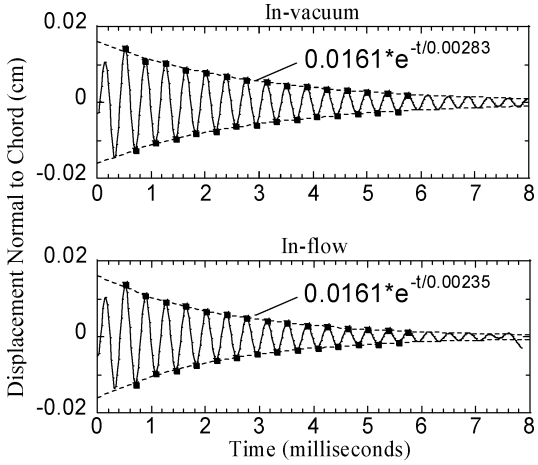

Fig. 9 Tip leading-edge displacement for torsion-only impulse after filtering.

Note that this interval gives over 20 data points for the curve fit. The amplitude A for the $Ae^{-t\omega_n\zeta}$ curve fit is fixed at 0.0354 cm, and ω_n is based on the bending mode frequency $f = 1310$ Hz. The least-squares fit gives an in-vacuum damping constant of $\zeta_v = 0.00207$ and an inflow damping constant $\zeta_{\text{tot}} = 0.00337$. When Eq. (22) is used, the aerodynamic damping for the first bending mode is $\zeta_a = 0.00130$.

Torsion-Only Impulse

At time $t = 0$, the blade is hit with the torsion mode impulse, Eq. (21). The resulting displacement of the tip leading edge normal to the tip chord is shown in Fig. 8 for both the in vacuum and the inflow cases. This signal is filtered as described earlier to extract only the torsion mode response, with this filtered signal shown in Fig. 9. The peaks and troughs of the curve within the interval 0.0005–0.006 s are extracted, and a curve fit is passed through them. Note that this interval gives over 20 data points for the curve fit. The amplitude A for the $Ae^{-t\omega_n\zeta}$ curve fit is fixed at 0.0161 cm, and ω_n is based on the torsion mode frequency $f = 2670$ Hz. The least-squares fit gives an in-vacuum damping constant of $\zeta_v = 0.0210$ and an inflow damping constant of $\zeta_{\text{tot}} = 0.0253$. When Eq. (22) is used the aerodynamic damping for the first torsion mode is $\zeta_a = 0.0043$. Thus, the aerodynamic damping for the first torsion mode is larger than the aerodynamic damping for the first bending mode.

Combined Bending and Torsion Impulse

The maximum blade displacement due to the bending and torsion impulses is small enough (tip displacements less than 1% chord) that nonlinear aerodynamic effects are negligible. Thus, the torsion and bending impulses can be applied simultaneously to determine the aerodynamic damping constants for both modes with just one simulation.

At time $t = 0$, the blade is hit simultaneously with the bending and torsion impulses for 100 μs. The resulting blade tip displacement normal to the chord is shown in Fig. 10 for both the in-vacuum and inflow cases. These curves are filtered, and the bending and torsion modal responses are separated (Fig. 11). The damping results from the curve fits are summarized in Table 4. The final aerodynamic damping constants for each mode are shown in the second last row, with the values found from the separate torsion and bending

Table 4 Damping constants for bending/torsion impulse with hourglass damping effect

Parameter	Bending mode	Torsion mode
Nominal Hourglass Damping		
A (in $Ae^{-t\omega_n\zeta}$), cm	0.0383	0.0129
Sampling interval, s	0.001–0.01	0.0005–0.006
ζ_v	0.00195	0.0214
ζ_{tot}	0.00321	0.0259
ζ_a (combined impulse)	0.00126	0.0045
ζ_a (separate impulses)	(0.00130)	(0.0043)
Low Hourglass Damping		
A (in $Ae^{-t\omega_n\zeta}$), cm	0.0384	0.0132
Sampling interval, s	0.001–0.01	0.0005–0.006
ζ_v	0.00101	0.0117
ζ_{tot}	0.00226	0.0159
ζ_a	0.00125	0.0042

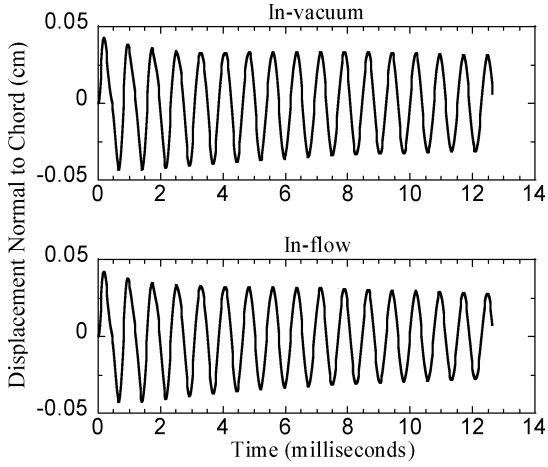

Fig. 10 Tip leading-edge displacement for bending/torsion impulse before filtering.

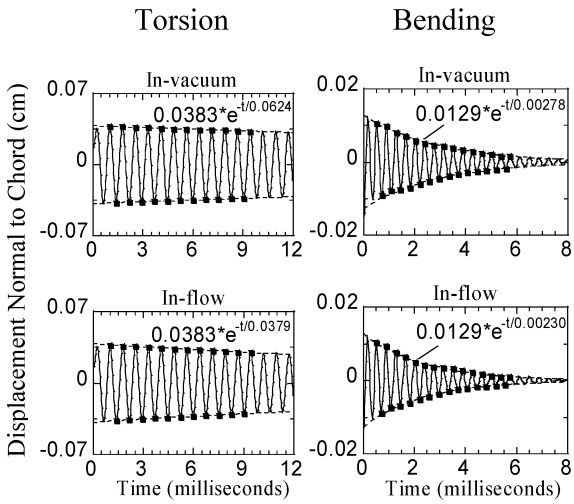

Fig. 11 Tip leading-edge displacement for bending/torsion impulse after filtering.

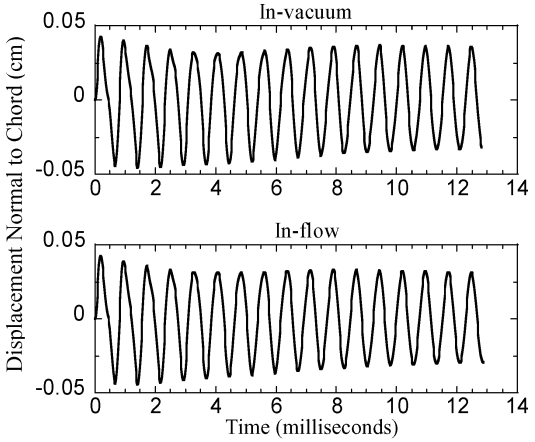

Fig. 12 Tip leading-edge displacement for low hourglass damping with bending/torsion impulse before filtering.

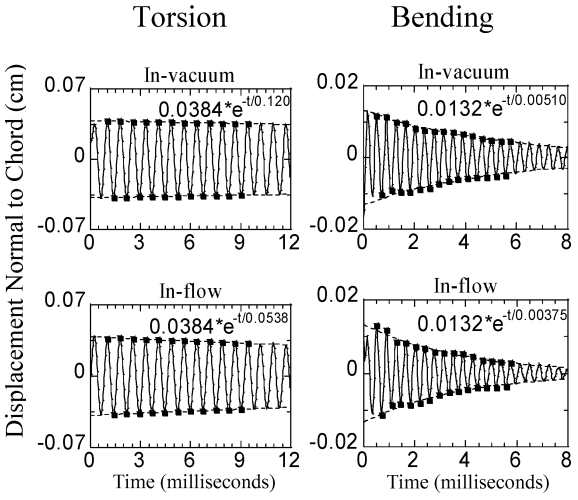

Fig. 13 Tip leading-edge displacement for low hourglass damping with bending/torsion impulse after filtering.

impulses in parentheses in the last row. The combined torsion/bending impulse produces bending and torsion damping constants approximately 3% lower and 5% larger, respectively, than the bending-only and torsion-only impulse results. These differences could be due to the inherent inaccuracies associated with curve-fitting discrete data points.

Reduced Hourglass Damping Case

As a self-consistency check on the results, the combined bending and torsion impulse case is repeated, except now the hourglass-damping coefficient [Q^{hg} in Eq. (15)] for the blade material is halved, being reduced from 0.10 to 0.05. This results in less overall damping for the blade, but should not change the aerodynamic damping.

The blade is again hit simultaneously with the bending and torsion impulse for 100 μs. The resulting blade tip displacement normal to the chord is shown in Fig. 12 for both the in-vacuum and inflow cases. These curves are filtered, and the bending and torsion modal responses are separated.

Figure 13 shows that the filtered torsion mode response is clearly less damped than the preceding case due to the decreased hourglass damping. The damping results from curve fits are summarized in Table 4. The final aerodynamic damping constants for each mode are shown in the last row. The low hourglass damping produces an aerodynamic damping constant for the bending and torsion modes approximately 1 and 7% smaller than the high hourglass damping results. Again, part of the difference is due to using a curve fit to describe a set of discrete data points. However, overall the results indicate that using the impulse technique is valid for extracting aerodynamic damping.

Summary

A novel approach has been developed to predict the aerodynamic damping of multiple vibration modes from two time-domain flow simulations, one with the blading in a vacuum and one with the blading in flow. This is accomplished by implementing a coupled interacting fluid–structure analysis that enables the same finite element method to model both the fluid and the structure. Thus, the exchange of energy and momentum across the fluid–structure boundary is not prone to phase-lagging errors that tend to act as energy sources or sinks at the fluid–structure boundary. This approach is then demonstrated by predicting the aerodynamic damping of a modern transonic compressor rotor.

The blading is first impulsed in its first bending and first torsion modes in a vacuum. It is then immersed in the design-point flowfield and impulsed in its first bending and first torsion modes again. Signal-processing tools applied to the predicted blade response time history extract the difference in the decay rate of both modes.

The results show that, for this rotor, the aerodynamic damping for the first bending mode is less than the aerodynamic damping for the first torsion mode. The feasibility of extracting the aerodynamic damping for several modes during one simulation was demonstrated by first running the simulations separately and then simultaneously. The resulting aerodynamic damping constants for the modes are very similar. A self-consistency check was performed by simulating the same case with different hourglass viscosity coefficients. The aerodynamic damping was not changed significantly by this change in hourglass viscosity, as expected.

The approach developed herein of modeling fluid–structure interactions in turbomachinery is consistent because the blade and fluid are modeled with the same numerical scheme. As computers become larger and faster, it is likely that this consistent approach will become the method of choice.

Acknowledgments

This research was sponsored, in part, by the Department of Energy, Accelerated Strategic Computing Initiative Program, Contract LG-6982. This support is most gratefully acknowledged.

References

[1]Bendiksen, O. O., "A New Approach to Computational Aeroelasticity," AIAA Paper 91-0939, April 1991.

[2]Bendiksen, O. O., "Eulerian–Lagrangian Simulations of Transonic Flutter Instabilities," Aeroelasticity and Fluid Structure Interaction Problems, Vol. 44, Aerospace Div., American Society of Mechanical Engineers, Fairfield, NJ, 1994, pp. 197–231.

[3]Hallquist, J. O., "Theoretical Manual for DYNA3D," Lawrence Livermore Lab., Rept. UCID-19401, Livermore, CA, March 1983.

[4]Gottfried, D. A., "Simulation of Fluid–Structure Interaction in Turbomachines," Ph.D. Dissertation, Dept. of Mechanical Engineering, Purdue Univ., West Lafayette, IN, May 2000, pp. 85–90.

[5]Noh, W. F., "Numerical Methods in Hydrodynamic Calculations," Lawrence Livermore Lab., Rept. UCRL-52112, Livermore, CA, June 1976, pp. 52, 58.

[6]Panton, R. L., *Incompressible Flow*, 1st ed., Wiley, New York, 1984, p. 61.

[7]Flanagan, D. P., and Belytschko, T., "A Uniform Strain Hexahedron and Quadrilateral with Orthogonal Hourglass Control," *International Journal for Numerical Methods in Engineering*, Vol. 17, No. 5, 1981, pp. 679–706.